GEOPHYSICS, VOL. 79, NO. 3 (MAY-JUNE 2014); P. E137–E148, 18 FIGS., 1 TABLE.
10.1190/GEO2013-0233.1

An approximate 3D computational method for real-time computation of induction logging responses

Silvian Bensdorp[1], Steen A. Petersen[2], Peter M. van den Berg[3], and Jacob T. Fokkema[3]

ABSTRACT

Over many years, induction logging systems have been used to create well formation logs. The major drawback for the utilization of these tools is the long simulation time for a single forward computation. We proposed an efficient computational method based on a contrast-type of integral-equation formulation, in which we applied an approximation for the 3D electromagnetic field. We assumed that the dominant contribution in the integral equation is obtained by the contribution around the singularity of Green's kernel. It is expected that the approximation yields reliable results when the (homogeneous) background conductivity around the logging tool is close to the actual conductivity at the location of the tool. We have developed a data-driven method to determine this background conductivity from the dominant part of the measured coaxial magnetic fields, which are mainly influenced by the conductivity at the tool sensors. For a synthetic model, the results were compared to the ones of a rigorous solution of the integral equation and show a good simulation response to small-scale variations in the medium. Further, the method was used to simulate the response of a realistic reservoir model. Such a model is created by a geological modeling program. We concluded that our approximate method was able to improve the approximation results in highly heterogeneous structures compared to the Born approximation and provide an effective medium-gradient around the tool. Our method, based on the wavefield approximation, also estimates the error, and hence yields a warning when the method becomes unreliable.

INTRODUCTION

In the oil industry, induction logging is a relevant method to discriminate between hydrocarbon-bearing and water (or shale)-bearing zones in the subsurface. Theoretical principles of the induction-logging method in some relatively simple canonical configurations can be found in Kaufman et al. (2003), whereas some more advanced and industry-focused examples can be found in Anderson (2001). The physical principle underlying the method is to probe the differences in electrical conductivity between the different zones. When an induction tool is lowered in a borehole, the electromagnetic field of the magnetic-dipole source(s) in the tool induces electrical currents in the subsurface formation. These induced currents contribute to the measured response in the magnetic-dipole receiver(s), which are also located in the tool some distance apart from the magnetic-dipole source(s). The interpretation of the measured response in terms of the formation conductivity gives in principle an indication for the location of the hydrocarbon bearing zones.

The present paper relates to a method for the approximation of the system response of an induction logging tool for the purpose of the analysis or synthesis of realistic earth conductivity configurations. The method aims to approximate in a reliable and computational fast way the response of a logging tool along an arbitrarily prescribed borehole trajectory in a full 3D-earth model, such that different realizations of borehole trajectories and earth models can be evaluated effectively. From a physical point of view, current logging tools consist of several magnetic-dipole sources (source coils) located at the tool axis in a direction of the tool axis and several magnetic-dipole receivers (receiver coils) located at the tool axis in an arbitrary orientation. The computation of the response of a logging tool in a 3D-inhomogeneous medium requires a full 3D

Manuscript received by the Editor 24 June 2013; revised manuscript received 30 October 2013; published online 2 May 2014.
[1]Delft University of Technology, Department of Geoscience and Engineering, Delft, The Netherlands. E-mail: s.bensdorp@tudelft.nl.
[2]Statoil ASA, Bergen, Norway. E-mail: steap@statoil.com.
[3]Delft University of Technology, Laboratory of Acoustical Wavefield Imaging, Delft, The Netherlands. E-mail: p.m.vandenberg@tudelft.nl; j.t.fokkema@tudelft.nl.

code based on the Maxwell equations. Although these codes, e.g., contrast-type of integral-equation methods (e.g., Avdeev et al., 2002; Zhang and Liu, 2003; Avdeev and Knizhnik, 2009; Nie et al., 2013), finite-element methods (e.g., Nam et al., 2013), and finite-difference methods (e.g., Newman and Alumbaugh, 2002; Weiss and Newman, 2002; Davydycheva et al., 2003, 2009), are nowadays available or becoming available, the computational burden is too large to carry out computations for different realizations of borehole trajectory and realistic earth models in a time-efficient matter. Hence, an effective approximate model that includes all the necessary physics is required. Direct linearization of the problem, assuming that the actual electric field in the domain of observation is equal to the background field, the so-called Born approximation, is too crude. Although there are several extensions to the Born approximation (e.g., Zhdanov et al., 2000; Tseng et al., 2003; Abubakar and Habashy, 2005), these methods rely in someway on the appliance of the integral operator. This is a computational intensive procedure and requires a regular structure of the simulation domain.

The logging response encompasses measurements of an induced magnetic field along a trajectory through a 3D-inhomogeneous medium for some prescribed frequency of operation. The method allows for the definition of an arbitrarily curved logging trajectory along which the electromagnetic response is computed. In our analysis, the borehole trajectory is replaced by locally straight line segments. Along each line segment, the electromagnetic field strength is only significant within a 3D volumetric window of limited dimensions. During the computation, the window can move and turn as it follows the trajectory. The size of this window of observation depends on the frequency of operation and the local electrical conductivity of the earth formation around the tool. For simplicity, we choose not to compensate for secondary borehole effects such as the effect of steel casing of the borehole (Kim and Lee, 2006), or induction tool eccentricity (Lovell and Chew, 1990).

We select the contrast-type of integral equation as mathematical tool to formulate our logging problem at hand. However, in each reduced window, a homogeneous background medium may be chosen, in which the electromagnetic field in this background medium is denoted as the primary electromagnetic field. In each local window, this primary electromagnetic field may be obtained directly from a simple closed-form expression. Within each window, a background medium should be chosen in such a way that the changes of the actual conductivity with respect to the one of the chosen background are as small as possible. One way to obtain such conductivity background is to average either the synthesized or a priori defined conductivity around the tool domain. In the present paper, we propose a data-driven determination of the local effective homogeneous background medium using the measurements from at least two axial-source coils and two axial-receiver coils. The background conductivity is determined by assuming that the measured fields may be approximated by the primary fields only.

Subsequently, the electric currents due to the differences in the electrical conductivity with respect to the effective one of the background medium in the window under investigation are seen as contrast currents that generate a secondary field. In principle, this leads to contrast-type of integral-equation formulation (see, e.g., Ward and Hohmann, 1988; Van Bladel, 2007). The computational solution of this integral equation over the reduced 3D window requires too much of computational time for real-time processing steps of the well logs. However, in view of the reduced size of each local window and the relative small changes of the contrast in electrical conductivity with respect to the one of the matched homogeneous background, the interaction between different regions within the local window can be neglected and each contrasting region may be seen as a *single-spherical scatterer (SSS)* (Slob, 1994). This so-called SSS approximation is used advantageously to provide a simple and effective model for the true disturbance of the electromagnetic field by the contrasting conductivity in the reduced window. The initial ideas of the present method are published as a patent application (Petersen et al., 2012b). By comparing the results of this approximation with the results obtained from the rigorously solved integral equations, we show the present approximation, but not guaranteed to give a better approximation, holds a better accuracy that is especially prevalent in a window with a highly heterogeneous conductivity distribution.

MATHEMATICAL FORMULATION

For purpose of mathematical description, let the spatial position in a Cartesian coordinate frame be given by $x = \{x_1, x_2, x_3\}$ and gradient by $\nabla = \{\partial_1, \partial_2, \partial_3\}$. Further, an electromagnetic time-dependence $\exp(-i\omega t)$ is assumed, where ω is the angular frequency and t is the time. In our induction-logging problem, we obtain a sequence of measurements of a controlled source generated magnetic field $H(x)$ along a curved borehole at different frequencies ω using an axial configuration of current loops.

The magnetic field and the electric field $E(x)$ are fully described by the Maxwell equations. Using the superposition principle, these fields can be recognized by their contributing sources. We separate the total field in a primary field $\{E^{\rm prm}, H^{\rm prm}\}$, generated by a magnetic-dipole source in a homogeneous medium, and a secondary field $\{E^{\rm scd}, H^{\rm scd}\}$. The latter is generated by the sum of all current sources that are induced by structural inhomogeneities in the surrounding medium. In view of the frequencies used and the physical medium properties, the dielectric displacement currents are negligible with respect to the electrical conduction currents. Then, the generated wavefields will exhibit a diffusive nature (Slob, 1994).

Our starting point is the contrast-type of integral-equation formulation based on the contrast in conductivity with respect to a constant background electric conductivity $\sigma_{\rm b}$, and the pertaining complex wavenumber $k_{\rm b} = (i\omega\sigma_{\rm b}\mu_0)^{\frac{1}{2}}$ for a diffusive wavefield, where μ_0 is the (constant) magnetic permeability of the subsurface. In view of the character of the diffusive wave, we restrict the region of computation to the domain where the secondary-field contributions are significant. To solve the forward scattering problem, for each set of measurements, we only have to solve this electromagnetic problem in the pertaining window. This procedure is repeated for each consecutive measurement as the tool progresses through a borehole (see Figure 1). For the nth measurement, it implies that we deal with the window domain Ω_n with borehole tangent $t_n(x)$. Within this geometric framework, we first discuss the integral equation that governs the local distribution of the electromagnetic field.

In a constant background of the window under observation the primary fields generated by a magnetic-dipole source are denoted as $\{E^{\rm prm}, H^{\rm prm}\}$. The secondary fields $\{E^{\rm scd}, H^{\rm scd}\} = \{E - E^{\rm prm}, H - H^{\rm prm}\}$, at position x, and generated by the contrasting conductivity within the finite window Ω_n, follow from the domain-integral representations (see Van Bladel, 2007):

$$E^{\mathrm{scd}}(x) = (k_{\mathrm{b}}^2 + \nabla\nabla\cdot)\int_{\Omega_n} g(x-x')\chi(x')E(x')\mathrm{d}x', \quad (1)$$

$$H^{\mathrm{scd}}(x) = \sigma_{\mathrm{b}}\nabla\times\int_{\Omega_n} g(x-x')\chi(x')E(x')\mathrm{d}x', \quad (2)$$

where Green's function is given by

$$g(x-x') = \frac{\exp\,(ik_{\mathrm{b}}|x-x'|)}{4\pi|x-x'|}, \quad (3)$$

and the electric contrast χ is given by

$$\chi(x) = \frac{\sigma(x)}{\sigma_{\mathrm{b}}} - 1. \quad (4)$$

Note that σ_{b} is constant in each window, but differs from window to window. The quantity $\chi(x)E(x)$ can be considered as the contrast current source distribution within the observational window. When the total field $E(x)$ is known in this window, the secondary field follows from the latter integral representations.

The total electric field $E(x)$ in the window of observation follows as the solution of the integral equation:

$$E(x) = E^{\mathrm{prm}}(x) + (k_{\mathrm{b}}^2 + \nabla\nabla\cdot)\int_{\Omega_n} g(x-x')\chi(x')E(x')\mathrm{d}x'. \quad (5)$$

From the exponential damping nature of Green's function it can be easily understood that first-order scattering effects will dominate the electromagnetic field inside a diffusive object. We use this property to derive a first-order approximate solution to the electromagnetic field, thereby severely reducing the computational complexity of the scattering problem at hand.

To derive this so-called SSS approximation, we observe that the major contribution of the integral on the right side of equation 5 comes from a small spherical domain $B(\delta)$ with radius δ around the singular point of the Green's function. Within this spherical domain, we assume that the contrast-source variation $\chi(x')E(x')$ is too small to matter. Hence, the integral equation is approximated by

$$E(x) \approx E^{\mathrm{prm}}(x) + \chi(x)E(x)(k_{\mathrm{b}}^2 + \nabla\nabla\cdot)\int_{B(\delta)} g(x-x')\mathrm{d}x'. \quad (6)$$

In the limit that the radius of the sphere $B(\delta)$ tends to zero, only the integral with the $\nabla\nabla\cdot$ operation in front yields a nonvanishing value (see Lee et al., 1980):

$$\lim_{\delta\to 0}\nabla\nabla\cdot\int_{B(\delta)} g(x-x')\mathrm{d}x' = -\frac{1}{3}I, \quad (7)$$

where I is the Kronecker dyadic. Hence, the integral equation simplifies to the relation:

$$E(x) \approx E^{\mathrm{prm}}(x) - \frac{1}{3}\chi(x)E(x), \quad (8)$$

with approximate solution

$$E(x) \approx \frac{3}{3+\chi(x)}E^{\mathrm{prm}}(x). \quad (9)$$

The SSS approximation will break down in domains of high-contrast variations in the vicinity of the tool. This also indicates that it is desirable to choose our contrast background conductivity in such a way as to minimize the contrast differences with respect to this background conductivity. In the limit that the absolute value of the contrast $\chi(x)\to 0$, we observe that we arrive at the so-called Born approximation $E(x)\approx E^{\mathrm{prm}}(x)$, which is the linearization of the scattering problem.

Finally, it is noted that we need the expressions for the primary electric and magnetic field in the background medium with conductivity σ_{b}. We assume that the source at a position x^S may be approximated by a magnetic-dipole source with magnetic moment M. Then, these expressions are (see Van Bladel, 2007)

$$E^{\mathrm{prm}}(x,x^S) = i\omega\mu_0\nabla g(x-x^S)\times M(x^S), \quad (10)$$

$$H^{\mathrm{prm}}(x,x^S) = (k_{\mathrm{b}}^2 + \nabla\nabla\cdot)g(x-x^S)M(x^S), \quad (11)$$

where μ_0 is the (constant) permeability of free space.

Total magnetic field at the receiver

The total magnetic field at any receiver point x^R is given by

$$H(x^R,x^S) = H^{\mathrm{prm}}(x^R,x^S) - \sigma_{\mathrm{b}}\int_{\Omega}[\nabla g(x-x^R)]\times\chi(x)E(x,x^S)\mathrm{d}x. \quad (12)$$

If the source and the receiver are polarized in the same direction as the source-receiver axis, a typical configuration encountered in induction logging systems, the magnetic primary field at the receiver point is obtained as

$$H^{\mathrm{prm}}(x^R,x^S) = \left(\frac{2}{|x^R-x^S|^2} - \frac{2ik_{\mathrm{b}}}{|x^R-x^S|}\right)g(x^R-x^S)M(x^S). \quad (13)$$

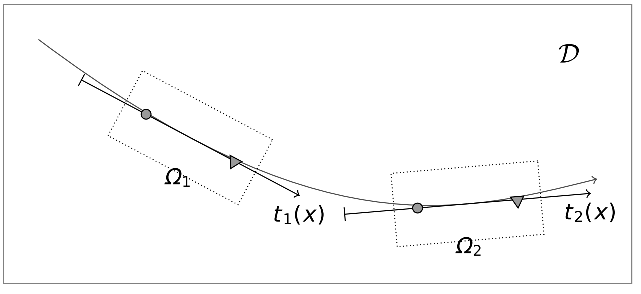

Figure 1. Induction logging configuration as assumed in our research. We consider multiple (overlapping) windows along the wellbore trajectory. Sources and receivers, indicated by the dots and the triangles, are both in the same window for a single spatial measurement point.

We substitute the SSS approximation of equation 9 for the electric field in the integral of equation 12. Subsequently, we use equation 10 to obtain the system response using the SSS approximation as

$$H(x^R,x^S) = H^{\mathrm{prm}}(x^R,x^S) - k_\mathrm{b}^2\int_\Omega[\nabla g(x-x^R)] \times[\nabla g(x-x^S)\times M(x^S)]\frac{3\chi(x)}{3+\chi(x)}\mathrm{d}x. \quad (14)$$

For later convenience, we give the expressions for the three components of the secondary field H_1^{scd}, H_2^{scd}, and H_3^{scd} when we deal with a source dipole with magnetic moment $M(x^S)=M(x^S)i_3$. They follow directly from equation 14 as

$$H_1^{\mathrm{scd}}(x^R,x^S) = -M(x^S)k_\mathrm{b}^2\int_\Omega \partial_3 g(x-x^R)\partial_1 g(x-x^S)\kappa(x)\mathrm{d}x, \quad (15)$$

$$H_2^{\mathrm{scd}}(x^R,x^S) = -M(x^S)k_\mathrm{b}^2\int_\Omega \partial_3 g(x-x^R)\partial_2 g(x-x^S)\kappa(x)\mathrm{d}x, \quad (16)$$

$$H_3^{\mathrm{scd}}(x^R,x^S) = M(x^S)k_\mathrm{b}^2\int_\Omega K_{\mathrm{axial}}(x^R,x^S,x)\kappa(x)\mathrm{d}x, \quad (17)$$

where

$$K_{\mathrm{axial}}(x^R,x^S,x) = \partial_1 g(x-x^R)\partial_1 g(x-x^S) + \partial_2 g(x-x^R)\partial_2 g(x-x^S), \quad (18)$$

and the effective contrast

$$\kappa(x) = \frac{3\chi(x)}{3+\chi(x)}. \quad (19)$$

As opposed to the linearized Born approximation, the effective contrast, as expressed in the fraction, is bounded.

Data-driven background

To facilitate the computations, we need a good estimation of the background conductivity in each window of computation. We propose a method to quickly obtain a good estimate for a background conductivity using multiple sources and receivers. Suppose we have a generic instrument with at least two coaxial sources and two coaxial receivers along the tool axis. Both sources and receivers are grouped together spatially (see Figure 2).

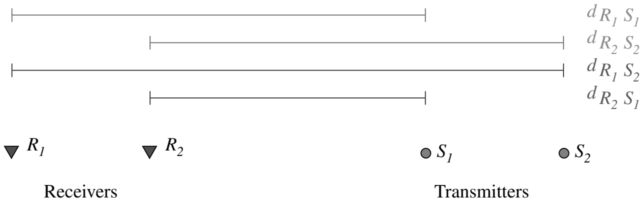

Figure 2. Configuration of a logging system able to derive a background conductivity.

The major parts of the magnetic fields generated and received by the coaxial source and receiver dipoles consist of the primary magnetic field. In each window of observation, we introduce a local coordinate system, in which the x_3-axis coincides with the tool axis. Hence, we assume that

$$H_3^{\mathrm{data}}(x^R,x^S)\approx H_3^{\mathrm{prm}}(x^R,x^S). \quad (20)$$

The primary field is controlled only by two parameters, the distance between source and receiver and the wavenumber k_b. For a source and receiver both polarized in the coaxial direction, the primary field is given by equation 13. In a single measurement, we deal with a constant background within the window of observation. From Figure 2, we observe that the sum of the distances $d_{R_1S_2}+d_{R_2S_1}$ is equal to the sum of the distances $d_{R_1S_1}+d_{R_2S_2}$. The equivalence of the sum of distances is the key of our method. By an appropriately chosen ratio of the data, we eliminate the unknown source- and receiver-dipole moments. We combine the data for the pair of source and the pair of receivers as follows

$$\eta = \left(\frac{d_{S_1R_1}d_{S_1R_2}}{d_{S_1R_1}d_{S_1R_2}}\right)^2\frac{H_3^{\mathrm{prm}}(x^{R_1},x^{S_1})H_3^{\mathrm{prm}}(x^{R_2},x^{S_1})}{H_3^{\mathrm{prm}}(x^{R_1},x^{S_2})H_3^{\mathrm{prm}}(x^{R_2},x^{S_2})}, \quad (21)$$

in which, we have replaced the data by the primary fields. We group the arguments of the exponent in the expressions of the primary fields (13) such that they become equivalent on both sides of the fraction, thereby elimination any dependency of η on $g(x^S-x^R)$. In this way, we end up with a quadratic equation for k_b, viz.

$$(-d_{R_1S_1}d_{R_2S_2}+\eta d_{R_1S_2}d_{R_2S_1})k_\mathrm{b}^2 + [i(d_1+d_2)(\eta-1)]k_\mathrm{b}+1-\eta=0. \quad (22)$$

For picking the correct branch, we need to pick a "physical" solution, i.e., the solution lying in the first quadrant of the complex plane. In the event, both solutions fall in the first quadrant, we will allow both of them. If no solution falls in the first quadrant, our assumption (equation 20) has diverged too much to give any meaningful contribution and the estimate has to be discarded. In case, there are more sources and/or receivers within the window of computation, multiple estimates for the background conductivity can be obtained, making the procedure more robust to false estimates and nonphysical characteristics of the obtained parameter. Once, we have a multitude of estimates for k_b, we take the average of the real part of all estimated wavenumbers that are clustered together. To find such cluster, we iteratively discard the wavenumber that is furthest away from the estimate ensemble mean. This process is continued until all wavenumber estimates fall within a predefined distance from the mean, or until our procedure is exhausted (that is, there are only two estimates left). The size of the final ensemble is used to generate a background wavenumber, as well as the ratio between the real and imaginary part, give an indication of the quality of the obtained wavenumber estimate.

For a perfect match, such as in a homogeneous medium, the physical properties that the real part of k_b will be equivalent to the imaginary part are maintained. In case, no estimate can be obtained, one can, as a last resort, interpolate the background conductivity numbers from neighboring windows, provided that these can generate an estimate.

Finally, we note that after determination of the background conductivity in a particular window, the magnetic-dipole moment $M(x^S)$ of the coaxial sources can be estimated using equations 13 and 20.

In a synthetic forward problem, the medium properties are known. We take advantage of this information by choosing our background conductivity σ_b in a way to minimize the overall contrast. A minimal contrast will lead to a more correct approximation, as well as a faster convergence for the integral-equation method. Our minimization is done by equating the background conductivity to the harmonic mean of the conductivity distribution of the pertaining window. Figure 3 demonstrates the impact of a piecewise constant background throughout the trajectory. It is observed that such variable adaptive background leads to smaller errors in the SSS approximation, more so when the adapted conductivity deviates from an average valued background conductivity. This behavior is to be expected because the part of the integral equation that is discarded in the SSS approximation is adaptively minimized. As our variable selection of the background conductivity is not necessarily the optimal background conductivity, we observe that the constant background at specific points leads to a smaller error than the variable background.

Gradient in the tool direction

For geosteering purposes, we need a first impression of the medium characteristics around a tool. A typical commercial tool can make a small number of measurements per fixed position. Therefore, a simple characterization of the medium should be made. In the present paper, we propose that the medium characterization consists of an estimate for the gradient transverse to the drilling and the gradient in the drilling direction.

For simplicity, let us assume there is a constant gradient of the effective medium in a window in the drilling direction. This is the gradient in the x_3-direction of a local coordinate system of the window. Because the transverse receiver dipoles at the axis of the tool do not measure any transverse component of the primary wave excited by a coaxial dipole source, we now focus on equation 15. Using integration by parts, we obtain

$$\begin{aligned} H_1^{\mathrm{scd}}(x^R,x^S)/M(x^S) = {} & k_b^2 \int_\Omega g(x-x^R)\partial_1\partial_3 g(x-x^S)\kappa(x)\mathrm{d}x \\ & + k_b^2 \int_\Omega g(x-x^R)\partial_3 g(x-x^S)\partial_1\kappa(x)\mathrm{d}x \\ & + k_b^2 \int_\Omega \partial_3[g(x-x^R)\kappa(x)\partial_1 g(x-x^S)]\mathrm{d}x. \end{aligned} \tag{23}$$

The first integral has an antisymmetric kernel, in the x_1- and x_3-directions, and therefore for small varying κ we choose to neglect it. Using Gauss' theorem, the third integral can be written as boundary integral at infinity and may be ignored because at infinity the diffusive electromagnetic field will decay exponentially to zero. Assuming that the $\partial_1\kappa(x)$ term does not effectively depend on x in a window of observation, we can obtain the effective gradient from equation 15 as

$$\partial_1\kappa = \frac{H_1^{\mathrm{scd}}(x^R,x^S)/M(x^S)}{k_b^2 \int_\Omega g(x-x^R)\partial_3 g(x-x^S)\mathrm{d}x}. \tag{24}$$

Starting again from equation 15, one could argue that using this approach it would also be possible to integrate by parts the ∂_1 term. This will result in a symmetric field along the (x_2,x_3)-plane at the center between the involved source and receiver. Numerical tests indicate that this will not lead to a valid and reliable approximation for the gradient in the x_1-direction such as we have done in the transverse case for the x_3-direction.

Because our approach relies on a rather coarse approximation, we balance out the error by using multiple transducer pair locations within the window of computation. We minimize the discrepancy in equation 24 by choosing

$$\partial_1\kappa = \frac{\sum_I [H(x^{R_I},x^{S_I})/M(x^{S_I})]^* (k_b^2 \int_\Omega g(x-x^{R_I})\partial_3 g(x-x^{S_I})\mathrm{d}x)}{\sum_I |k_b^2 \int_\Omega g(x-x^{R_I})\partial_3 g(x-x^{S_I})\mathrm{d}x|^2}, \tag{25}$$

where I is the index of all available transducer pair location and the asterisk denotes complex conjugate.

As argued, we cannot use the previous mechanism to obtain a gradient in the drilling direction. A way to circumvent this problem is to approximate the magnetic field on the tool axis using some kind of interpolation scheme. To obtain an estimate at the center of the window, the tool needs to have a symmetric layout around the window center. If multiple sources are present at equivalent but opposite side of the center, their estimated fields on the axis must be added to remove their spatial bias. In case the number of transmitters is larger than the number of receivers, we can interchange their function by the use of electromagnetic reciprocity. This procedure should be used with some care, as the strength of the interpolated field at the center of the window will be heavily influenced by the

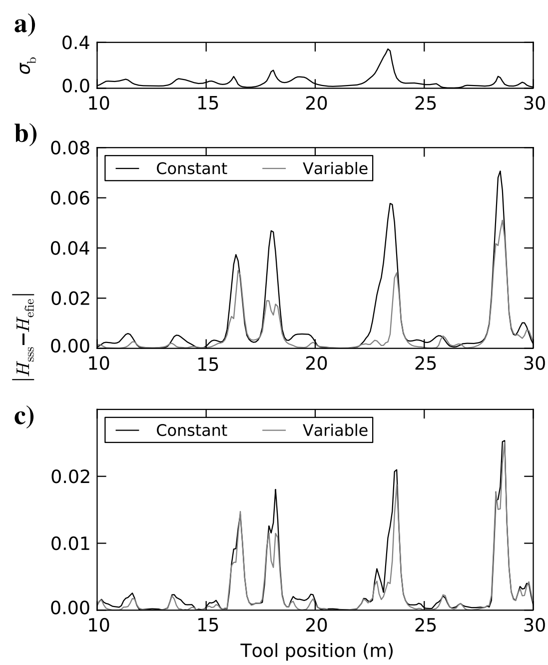

Figure 3. Absolute differences between the approximated magnetic field and the computed magnetic field at the receiver position for fixed constant σ_b and variable (piecewise constant) σ_b. (a) Piecewise variable background conductivity for comparison, (b) transverse polarization, and (c) coaxial polarization.

measured values near the vicinity of the center, and a single faulty measurement can spoil the entire gradient estimation. To remedy this, all measured values should be validated for physical consistency (larger source-receiver spacings result in smaller electromagnetic responses).

Finally, it is noted that we can also consider the data of a transversal receiver measuring H_2^{scd} only. The same analysis as for the H_1^{scd} component can be made and these extra results can be added to the minimization procedure of equation 25.

RESULTS

We test the SSS approximation for two cases. The first is a synthetic medium, showing the characteristics of the SSS approximation. The second case is a conductivity distribution model based on a North Sea production oil field. The conductivity model was created using the compound earth simulator (Petersen, 2004; Petersen et al., 2012a), a software tool for construction of geological models and the generation of synthetic data based on these models. Through this conductivity model, we put a realistic drilling trajectory path, and generate forward responses along this path.

SSS approximation

To estimate the appropriate window size, the maximum penetration depth of the tool for a specific frequency and background is required. The actual penetration depth will be a function of many parameters, and is in effect difficult to determine. To assist, one can compute, the transverse sensitivity kernel:

$$K_{tv} = \partial_3 g(x - x^R)\partial_1 g(x - x^S), \tag{26}$$

and the sensitivity kernel K_{axial}, given in equation 18, for all x in a particular window. The results for a source-receiver pair spaced 1 m apart are shown in Figure 4 for $\sigma_{\mathrm{b}} = 0.1$ and for a frequency of operation of 400 kHz and 2 MHz, respectively. These frequencies are typically found in a multitude of commercial induction logging tools, as 2 MHz is an approximate upper limit where conduction currents are 30–300 times larger than displacement currents, justifying the neglect of these displacement currents. We immediately observe the reduction in sensitivity for 2 MHz.

For a window size to reflect up to certain accuracy, we select a minimum sensitivity that we wish to be included into the results. The window should be large enough to encompass this sensitivity curve. If we use some kind of average in the window to select the background conductivity, this background conductivity itself will depend on the window size. This can be circumvented by calculating the average background conductivity σ_{b} only in some small "pre-window" where the sensitivity is high, and use this value for σ_{b} to compute the sensitivity ranges. From computations using the integral-equation method with windows encompassing sensitivities down to -80 dB, it is observed in some simple test scenarios that the magnetic field at the receiver is within 1% of the large window computation if the window encompasses the -50 dB curve.

Our test configuration is a purely synthetic model with moderate contrast values (see Figures 5 and 6). The change in contrast increases if the tool source position moves to the right, to simulate high-contrast values as well. We simulate the response of an induction tool in this medium along a line at $x_1 = 0$, and runs from $x_3 = 10$ to $x_3 = 30$. We sample the global medium around the tool and use a bilinear interpolation to map the global medium to a local window. To keep the model simple, the medium is 2D, but we keep the 3D electromagnetic field, the so-called 2.5D case. We take a mesh size of 0.030 m for the 2 MHz simulation and 0.068 m for the 400 kHz simulation. The window size in these example is $2.8 \times 2.8 \times 2.8$ m for the 2 MHz simulations, and $3.6 \times 3.6 \times 3.6$ m for the 400 kHz simulations. The tool is shifted 0.1 m per simulation point. Simulations were performed with a source-receiver spacing of 0.25 and 1.0 m, a distance typically encountered in commercial high-frequency induction logging tools. The results of these simulations are shown in Figures 7–10, where we plot the relative error of the magnetic field error with respect to the integral-equation solution. As the magnetic field computations follow directly from the (approximated) electric field, we shall first consider the error in the electric field estimates, which is the source of the error in the magnetic field approximations. We compute the normalized L_2 error in the electric field estimate on the windowed domain by

$$\mathrm{error}(E^{\mathrm{est}}) = \frac{\|E^{\mathrm{prm}} - \mathcal{G}(E^{\mathrm{est}})\|_2}{\|E^{\mathrm{prm}}\|_2}, \tag{27}$$

where the integral-equation operator as defined in equation 5 is represented by $\mathcal{G}$. We do not introduce any weighting for the spatial location of the electric field with respect to the receiver. Figure 11 shows the difference

$$\Delta_{\mathrm{err}} = \mathrm{error}(E^{\mathrm{Born}}) - \mathrm{error}(E^{\mathrm{SSS}}), \tag{28}$$

between the error of the Born approximation and the SSS approximation error computed using equation 27. A positive value thus indicates the SSS approximation yielding a smaller L_2 error than the Born approximation. It is clear that the SSS electric field estimate is almost always better than the Born approximation, more so when the structure heterogeneity in the window becomes more prevalent. As a separate test, we multiplied the error vector with a weighting matrix depending on the receiver distance, to emphasize the errors at physical locations that will have the most contribution to the magnetic field. This, however, seemed to have a negligible influence on the relative error performance.

We obtain this relative error of the magnetic field from the pertaining electric field approximation. For each component n, we define the error as

$$\mathrm{error}(H_n^{\mathrm{est}}) = \frac{|H_n^{\mathrm{approx}} - H_n^{\mathrm{efie}}|}{|H_n^{\mathrm{efie}}|}. \tag{29}$$

Here, we obtain the solution H_n^{efie} to a preconditioned integral equation iteratively, down to an error $<10^{-6}$ as defined in equation 27 using the generalized minimum residual algorithm (Saad, 2003).

It is noted that there is no significant upward trend in the relative error as the contrast fluctuations increase when progressing through the borehole. This contradicts our expectations, as high-contrast variations should result in stronger high order scattering, which the Born and the SSS approximation discard. Another more remarkable observation, is that for the coaxial polarized receiver the Born approximation tend to produce lower errors, whereas for the transverse polarized receiver the SSS approximation clearly outperforms the Born approximation for all four synthetic scenarios. These findings are supported by the log-mean values of the errors as presented in Table 1. This table also contains the standard deviations of the log errors. These show that, while the SSS approximation yields results that are overall worse for the coaxial receiver polarization, its results are much more stable as indicated by a lower log standard deviation. This is a clear advantage if the medium around the borehole trajectory contains a lot of variation in a short spatial interval.

From Table 1 it is further observed that the Born and the SSS approximation perform best when the distance between the source and receiver is small for the coaxial polarization, whereas for the transverse polarization a larger source-receiver spacing seems to generate better results. There seems to be no obvious relation between the source frequency and the relative error, although the numerical examples presented are too few to draw any conclusions.

To show the particular advantage of the SSS approximation, as a second example, we simulate a trajectory in a background medium of 0.01 S/m, penetrating a 0.25 m thick layer of 1.0 S/m at a 45° angle, with 0.25 m source-receiver spacing (see Figure 12). The results are shown in Figure 13. Here, we can clearly observe the benefit of the SSS approximation. As the window moves into the range of the layer, the contrast variation in the window becomes a prevalent influence on the magnetic field strength. From the figures, we observe that in these transition zones the SSS approximation yields

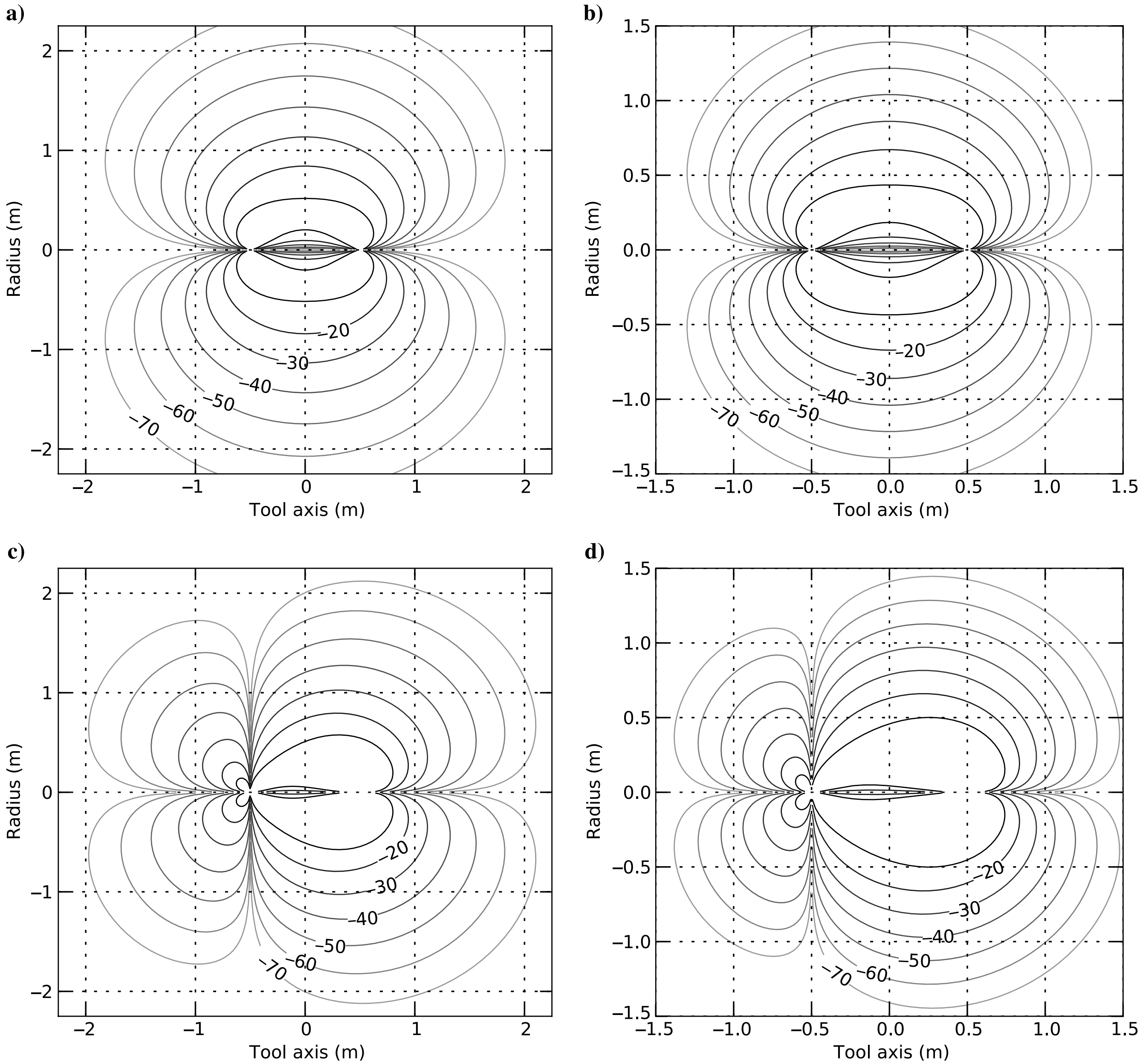

Figure 4. Tool sensitivity (in dB) for $\sigma_b = 0.1$ S/m and 1 m source-receiver spacing, M is the unit vector in the coaxial direction. (a) An axial transducer pair at 400 kHz, (b) an axial transducer pair at 2.0 MHz, (c) transverse transducer combination at 400 kHz, and (d) transverse transducer combinations at 2 MHz.

superior results. As we move away from the layer, or are in the middle of the layer, the difference between the Born approximation and the SSS approximation becomes smaller and there is less of a definite benefit for either of the two approximations.

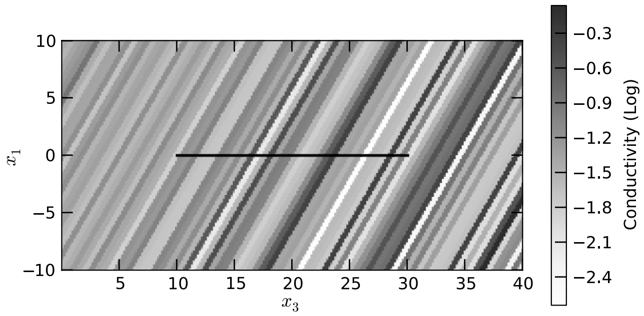

Figure 5. Used conductivity model (in log scale) for synthetic simulations. The borehole is at $x_1 = 0$ (radial direction), and runs from 10 to 30 m on the tool axis in the x_3-direction.

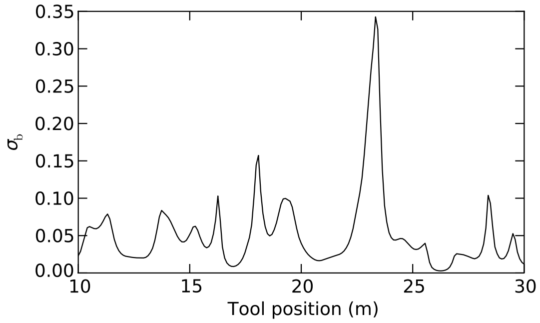

Figure 6. Background conductivity σ_b in S/m used for field calculations at the tool location.

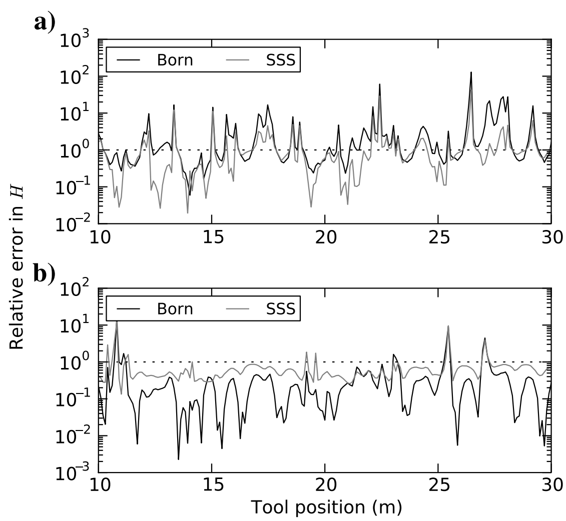

Figure 7. Short source/receiver spacing (0.25 m) magnetic field H^{scd} along the trajectory for a 400 kHz source. (a) Error for coaxial polarization configuration and (b) error for transverse polarization configuration.

Gradient estimation

To demonstrate the effect of the effective gradient, we use the same model as the second synthetic test (Figure 12), the penetration of a 0.25 m thick layer at an 45° angle with conductivity 0.2 S/m. For stability, we use two sources and four receivers to generate eight data pairs. The sources are located at −0.5 and +0.5 m, the receivers are spaced in between at −0.16 and +0.16 m. The data are generated using the integral-equation approach to simulate a more realistic data set. To scale the gradient to the background, we keep the background constant throughout the trajectory to obtain a gradient relative to this constant background. In Figure 14, we

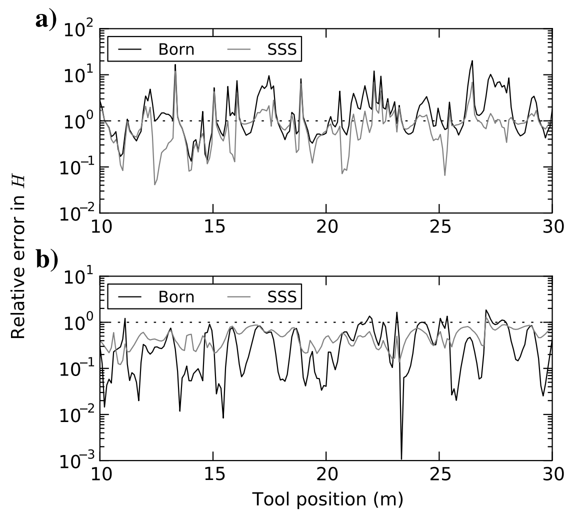

Figure 8. Short source/receiver spacing (0.25 m) magnetic field H^{scd} along the trajectory for a 2 MHz source. (a) Error for coaxial polarization configuration and (b) error for transverse polarization configuration.

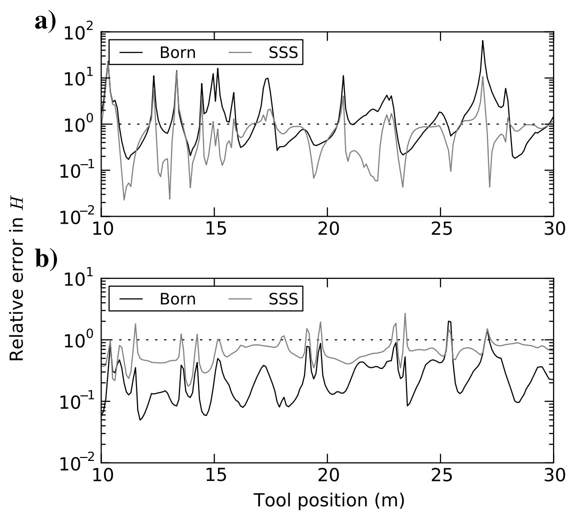

Figure 9. Long source/receiver spacing (1.0 m) magnetic field H^{scd} along the trajectory for a 400 kHz source. (a) Error for coaxial polarization configuration and (b) error for transverse polarization configuration.

observe the behavior of the gradient estimation in a simple setting. When approaching the dipped layer, the gradient increases, whereas when the tool leaves the high-conductivity layer the gradient changes sign and decreases until the layer is out of range. In the middle part, as the background conductivity changes, so does the gradient with respect to this background. This causes the oscillation observed in the middle segment.

Field example: North Sea production field

To verify our approach in a more realistic setting, we deploy a conductivity model of a part of the North Sea field created using the compound earth simulator (Petersen et al., 2012a), see Figure 15. The model section that we will use to test our algorithms stretches over a distance of about 1100 m. The used drill path in our simulation resembles a true production drilling path, thereby generating equivalent logs as could be obtained from calibrated field measurements. The formation has a high conductivity at top and floor representing shale layers, and an increasing conductivity toward the bottom of the reservoir simulating rising water levels in the lower parts.

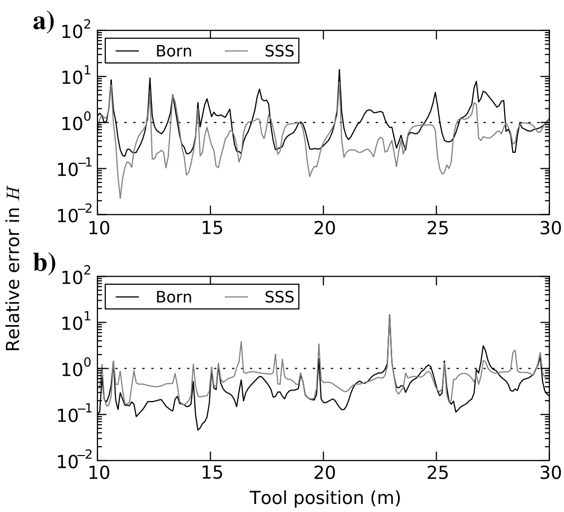

Figure 10. Long source/receiver spacing (1.0 m) magnetic field H^{scd} along the trajectory for a 2 MHz source. (a) Error for coaxial polarization configuration and (b) error for transverse polarization configuration.

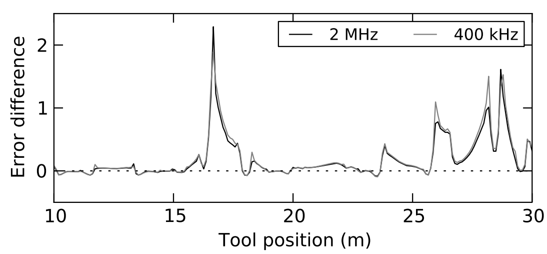

Figure 11. Error difference of the estimated electric field for the SSS approximation and the Born approximation. A positive value implicates the SSS approximation yields a better approximation than the Born approximation for the total electric field.

We simulate the trajectory response for the short source-receiver spacing (0.25 m) for a short part of the trajectory, between lateral distances 1020 and 1180 m. This section was selected because it contains some high-contrast regions, where the SSS approximation, as shown in the synthetic example, is of most benefit. Computations over the rest of the trajectory show no direct preference for the SSS approximation. The magnetic fields approximated by the Born approximation are generally too weak in the trajectory, the SSS approximation makes this behavior worse if a low background conductivity is selected. Simulations are done for 400 kHz and 2 MHz. We observe a behavior similar as with the purely synthetic models. In regions with a low contrast variation, the Born and the SSS approximation perform approximately equal, depending on the polarization type. In the regions with a high-contrast variability, such as when the two clay columns in the North Sea model between 1000 and 1200 m are penetrated, the SSS approximation performs clearly much better than the Born approximation.

Figure 16 shows the estimated background conductivity along the well path. As expected the background conductivity increases in higher conductivity zones. In highly heterogeneous zones, the error of the estimation increases due to the effective lack of a coherent background structure. This is a useful indication as a high error can be used as an indicator for shale approaches of the well path.

The transverse gradient measures as we have defined pick up almost all major structures changes within their range, as can be

Table 1. The log-mean and log standard deviation of the relative absolute for different responses in the synthetic example (ss, short source-receiver spacing; ls, long source-receiver spacing).

	Log mean		Log std. dev.	
	Born	SSS	Born	SSS
400 kHz coaxial (ss)	−1.8012	−0.5685	1.3426	0.5493
400 kHz coaxial (ls)	−1.5139	−0.4659	0.7187	0.4174
400 kHz transverse (ss)	0.2742	−0.4544	1.2055	1.2216
400 kHz transverse (ls)	0.1021	−0.6057	1.1268	1.1296
2 MHz coaxial (ss)	−1.4656	−0.7803	1.2151	0.4558
2 MHz coaxial (ls)	−1.0719	−0.5703	0.8088	0.6154
2 MHz transverse (ss)	0.2187	−0.3811	0.9979	0.9072
2 MHz transverse (ls)	−0.1373	−0.7768	0.8870	0.9340

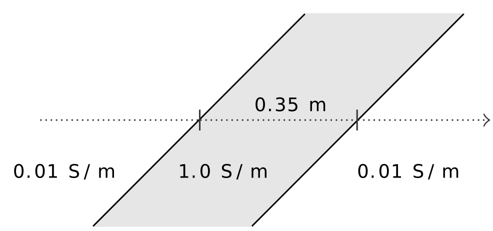

Figure 12. Canonical configuration with borehole (dotted line) passing through a high-conductivity layer (not in scale).

observed in Figure 17, that are caused by the tool approaching or penetrating shale deposits. Further, the lowering into the water saturated part (approximately between 1550 and 1700 m) of the formation is also visible in the gradient.

From Figure 18, we observe that the error becomes quite significant at some parts (e.g., from 1800 m onward). This effect is due to the low actual contrast and dominant layered structure of the medium, rendering such measures useless. To counter such behavior, we keep track of the background conductivity as well (see Figure 16) because a low background conductivity (such as in the order of 10^{-3} to 10^{-2}) indicates a homogeneous hydrocarbon bearing zone.

For our gradient estimate procedure, the frequency plays a crucial role as it controls the effective range of the tool as well as the sensitivity to details in the gradient reconstruction. As we take into account the responses at multiple frequencies, the different resulting gradients will give a good indication of the local variability of the medium. This is shown in Figure 17, where the tendencies of both curves coincide on most of the model. The responses diverge only in local highly heterogeneous structures.

Computational time

The full benefit of using the SSS approximation is obtained when there is a need to compute the response in a large amount of windows, such as response prediction for a proposed wellbore. To quantify this benefit, we compare the computational cost of the SSS approximation with the integral equation. The SSS approximation for a trajectory can be computed in order γN operations, where γ is the number of windows and N is the number of grid points. For the integral equation, the order of the computational cost is estimated by $\gamma(M(18N \log_2 N))$, where M is the number of iterations to solve the forward problem. The number of iterations M can be in the order of 2–7, depending on the particular characteristics of the conductivity distribution in the medium, as well as the discretization size of the simulation domain. If we assume $N = 3 \times 50^3$, the computation of the tool responses in a part of a borehole trajectory using the EFIE approximation takes over 10,000 times the computational time of the SSS approximation for average M. Experiments, however, show that our observation is conservative, as for our chosen N computational times in the order of seconds were observed for the SSS approximation on a standard desktop machine, whereas the EFIE requires multiple hours to complete. This is due to the more elaborate overhead of solving the integral equation.

CONCLUSION

We have introduced the SSS approximation for the diffusive electromagnetic field. As a closed-form expression, this allows for a fast computation of the magnetic field at any point in a predefined window illuminated by a source located in that window. Beside this

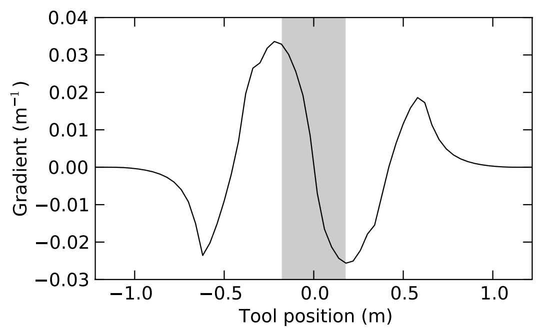

Figure 14. Gradient estimation of a simple dipped layer configuration at 2 MHz. The gray zone indicates the position the tool center is in the high-conductivity layer.

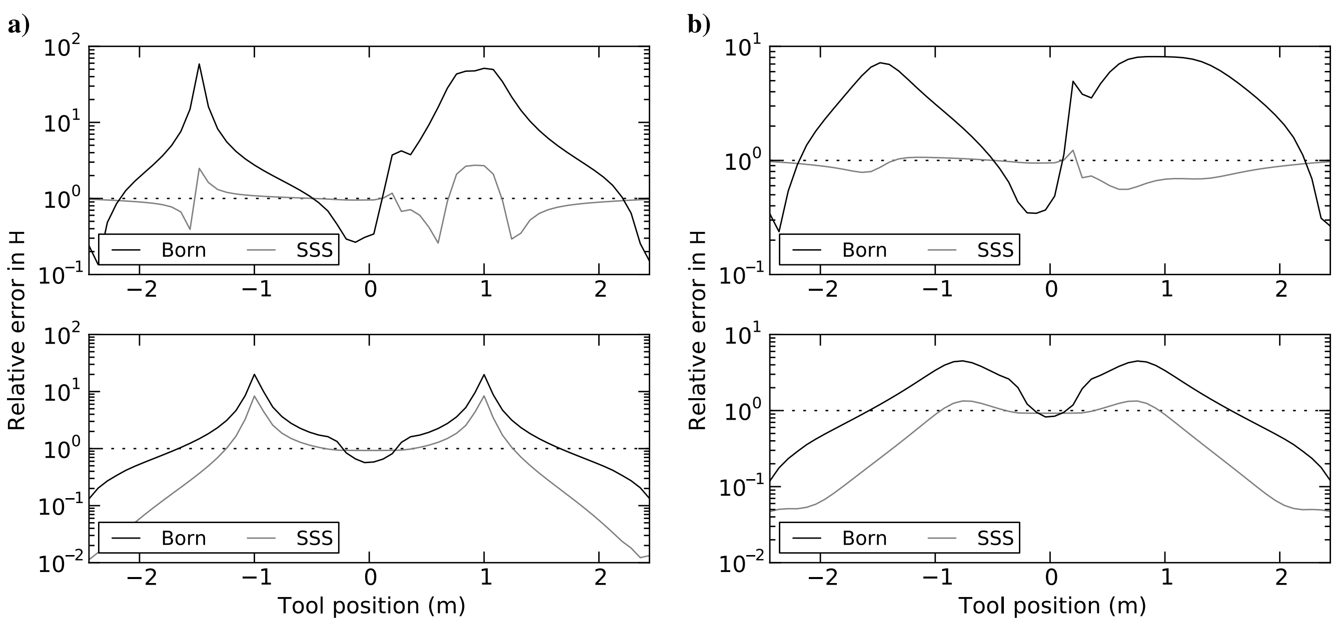

Figure 13. Coaxial error (top) and transverse error (bottom) for the magnetic field at the receiver for a canonical example of a 0.25 m thick layer penetration of 1.0 S/m under a 45° angle. (a) 400 kHz results and (b) 2 MHz results.

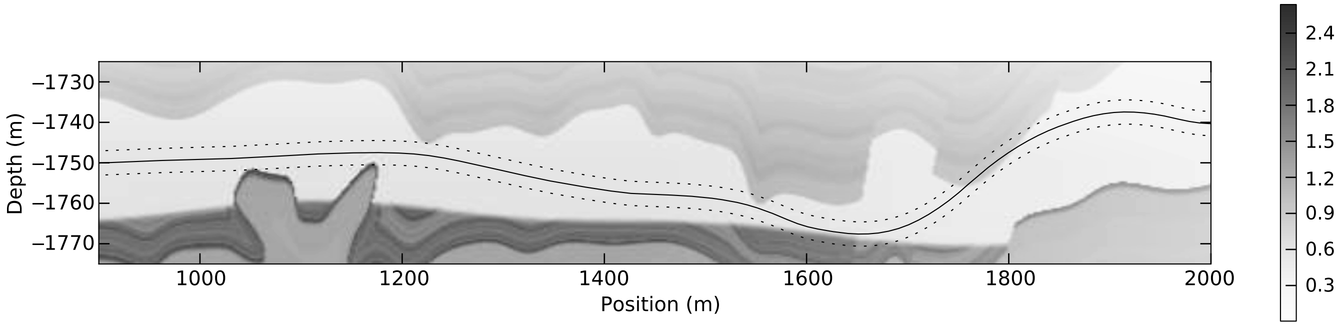

Figure 15. North Sea production field conductivity model (in S/m, log scale) used as a realistic scenario for a deepwater hydrocarbon reservoir. The solid line indicates the trajectory used to simulate the tool response. The dotted lines give a rough indication of the range of the tool at 2 MHz.

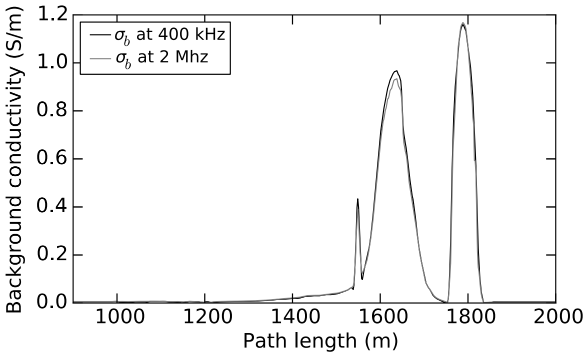

Figure 16. Background conductivity σ_b obtained from the total magnetic field data generated from the North Sea production field conductivity model.

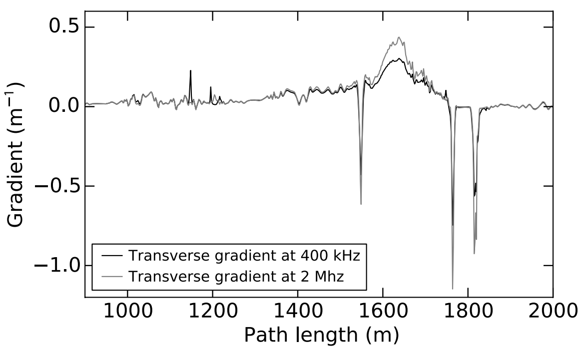

Figure 17. Estimated gradient in the transverse drilling direction along the trajectory in the North Sea reservoir model for 400 kHz and 2 MHz.

approximation, we deal with a moving window along the tool trajectory and a constant background conductivity in each specific window. The values of the window background conductivity vary along the tool path. This changing background conductivity in each window is recruited from the data itself. This data-driven background can improve the Born approximation, the SSS approximation and the convergence of the iterative solution of the integral-equation method. The approximations are particularly convenient to use as a forward model for synthesis purposes and as a model

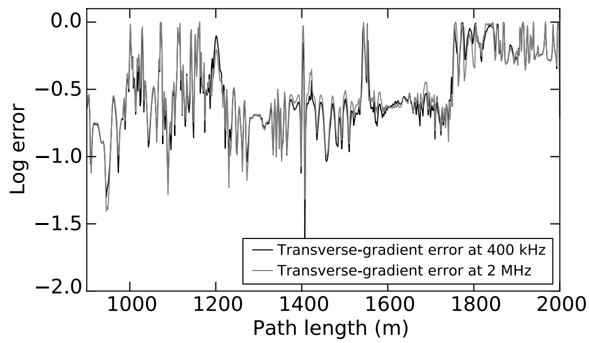

Figure 18. Error in the estimate of the transverse gradient $\partial\kappa/\partial x_3$.

for conductivity-inversion strategies. As industrial practice moves toward real-time processing and interpretation, a balance between accuracy and speed will be critical to support such a workflow.

We have shown that the SSS approximation is of particular benefit when simulating the response of a window with a highly heterogeneous contrast distribution. Further, from the synthetic examples, the transverse source-receiver polarization results with the SSS approximation tend to be overall better and more stable. For the North Sea model, no such apparent conclusion can be drawn.

The results from the North Sea conductivity model show that our methods can be used in a realistic configuration. We have observed that the simulated data resembles the geological variations in conductivity. These results are promising for real-time inversion strategies.

ACKNOWLEDGMENTS

The authors acknowledge Statoil ASA for financial support and permission to publish the North Sea production field conductivity model. The authors want to thank doctors Antonsen and Olsen for stimulating discussions and Avdeev and Kuvshinov for their clear comments that improved the original manuscript considerably.

REFERENCES

Abubakar, A., and T. M. Habashy, 2005, A Green function formulation of the extended Born approximation for three-dimensional electromagnetic modelling: Wave Motion, **41**, 211–227, doi: 10.1016/j.wavemoti.2004.05.011.

Anderson, B. I., 2001, Modeling and inversion methods for the interpretation of resistivity logging tool response: Ph.D. thesis, Delft University of Technology.
Avdeev, D., and S. Knizhnik, 2009, 3D integral equation modeling with a linear dependence on dimensions: Geophysics, **74**, no. 5, F89–F94, doi: 10.1190/1.3190132.
Avdeev, D. B., A. V. Kuvshinov, O. V. Pankratov, and G. A. Newman, 2002, Three-dimensional induction logging problems, Part I: An integral equation solution and model comparisons: Geophysics, **67**, 413–426, doi: 10.1190/1.1468601.
Davydycheva, S., V. Druskin, and T. Habashy, 2003, An efficient finite-difference scheme for electromagnetic logging in 3D anisotropic inhomogeneous media: Geophysics, **68**, 1525–1536, doi: 10.1190/1.1620626.
Davydycheva, S., D. Homan, and G. Minerbo, 2009, Triaxial induction tool with electrode sleeve: FD modeling in 3D geometries: Journal of Applied Geophysics, **67**, 98–108, doi: 10.1016/j.jappgeo.2008.10.001.
Kaufman, A. A., and Yu. A. Dashevsky, 2003, Principles of induction logging: Elsevier Science, vol. **38**, *of* Methods in Geochemistry and Geophysics.
Kim, H. J., and K. H. Lee, 2006, Electromagnetic fields in a non-uniform steel-cased bore-hole: Geophysical Prospecting, **54**, 433–439, doi: 10.1111/j.1365-2478.2006.00545.x.
Lee, S.-W., J. Boersma, C.-L. Law, and G. Deschamps, 1980, Singularity in Green's function and its numerical evaluation: IEEE Transactions on Antennas and Propagation, **28**, 311–317, doi: 10.1109/TAP.1980.1142329.
Lovell, L. R., and W. C. Chew, 1990, Effect of tool eccentricity on some electrical well-logging tools: IEEE Transactions on Geoscience and Remote Sensing, **28**, 127–136, doi: 10.1109/36.45750.
Nam, M. J., D. Pardo, and C. Torres-Verdin, 2013, Simulation of borehole-eccentered tri-axial induction measurements using a Fourier HP finite-element method: Geophysics, **78**, no. 1, D41–D52, doi: 10.1190/geo2011-0524.1.
Newman, G. A., and D. L. Alumbaugh, 2002, Three-dimensional induction logging problems, Part 2: A finite-difference solution: Geophysics, **67**, 484–491, doi: 10.1190/1.1468608.
Nie, X. C., N. Yuan, and R. Liu, 2013, A fast integral equation solver for 3D induction well logging in formations with large conductivity contrasts: Geophysical Prospecting, **61**, 645–657, doi: 10.1111/j.1365-2478.2012.01070.x.
Petersen, S. A., 2004, Optimization strategy for shared earth modeling: 66th Annual International Conference and Exhibition, EAGE, Extended Abstracts, P257.
Petersen, S. A., Ø. Hjelle, S. Hustoft, M. Houbiers, and R. Rasmussen, 2012a, A data-restoration and model-reconstruction workflow for simultaneous seismic interpretation and model building: 74th Annual International Conference and Exhibition, EAGE, Extended Abstracts, D036.
Petersen, S. A., P. M. van den Berg, and J. T. Fokkema, 2012b, Method of predicting the response of an induction logging tool: U.S. patent application WO2012103945.
Saad, Y., 2003, Iterative methods for sparse linear systems: SIAM.
Slob, E. C., 1994, Scattering of transient diffusive electromagnetic fields: Ph.D. thesis, Delft University of Technology.
Tseng, H.-W., K. H. Lee, and A. Becker, 2003, 3D interpretation of electromagnetic data using a modified extended Born approximation: Geophysics, **68**, 127–137, doi: 10.1190/1.1543200.
Van Bladel, J., 2007, Electromagnetic fields: John Wiley & Sons, IEEE Press, Series on Electromagnetic Wave Theory.
Ward, S. H., and G. W. Hohmann, 1988, Electromagnetic methods in applied geophysics, vol. 1: Theory: SEG, Investigations in Geophysics 2.
Weiss, C. J., and G. A. Newman, 2002, Electromagnetic induction in a fully 3-D anisotropic earth: Geophysics, **67**, 1104–1114, doi: 10.1190/1.1500371.
Zhang, Z. Q., and Q. H. Liu, 2003, Applications of the BCGS-FFT method to 3-D induction well logging problems: IEEE Transactions on Geoscience and Remote Sensing, **41**, 998–1004, doi: 10.1109/TGRS.2003.811547.
Zhdanov, M. S., V. I. Dmitriev, S. Fang, and G. Hursáan, 2000, Quasi-analytical approximations and series in electromagnetic modeling: Geophysics, **65**, 1746–1757, doi: 10.1190/1.1444859.